GEOPHYSICS, VOL. 88, NO. 1 (JANUARY-FEBRUARY 2023); P. WA105–WA114, 10 FIGS., 3 TABLES.
10.1190/GEO2022-0159.1

DOI:10.1190/geo2022-0159.1

Enhancing one-way wave equation-based migration with deep learning

Yuwei Yu[1], Yaxing Li[1], Xinming Wu[1], and Xiaofeng Jia[1]

ABSTRACT

One advantage of one-way wave equation-based migration is its low computational cost. However, due to the limited wavefield propagation angle, it is difficult to use one-way wave equation-based migration for high-precision imaging of structures with large inclinations due to issues such as inaccurate amplitudes and migration image artifacts. In addition, when the model has large horizontal velocity differences, it is difficult for the one-way wave propagator to calculate an accurate wavefield phase. Reverse time migration (RTM) based on the two-way wave propagator has a high resolution and avoids the issues associated with one-way wave propagators; however, it has a high computational cost in practical applications. We develop a convolutional neural network (CNN) application mode that improves one migration method by learning from another one and design a CNN with a structure similar to U-net that combines the advantages of both migration methods. The CNN label is the RTM result, and the corresponding input is the result of one-way wave migration with a generalized screen propagator (GSP). The trained CNN model improves the amplitude in the one-way wave migration image and removes the errors caused by large lateral velocity perturbations. Moreover, by maintaining the high migration calculation efficiency, our CNN model allows for a high resolution, few artifacts, and accurate images of steep structures in the one-way wave migration result. With our method, the accuracy of the one-way wave migration result is close to that of the RTM result. The use of GSP-based migration in our CNN model rather than conventional RTM to generate prospecting images can considerably reduce the calculation costs.

INTRODUCTION

Seismic migration is a detection technique that returns the energy of recorded data to its original position. The returned energy creates an image that outlines underground structures; these migration images can be used for resource exploration and disaster prevention. After years of research, various migration methods (Shragge and Shan, 2008; Etgen et al., 2009; Leveille et al., 2011) have been proposed in response to different detection requirements. Among them, reverse time migration (RTM) based on the two-way wave propagation operator (Baysal et al., 1983; McMechan, 1983) is preferred by researchers because of its outstanding imaging performance. However, in prestack RTM, the zero-lag crosscorrelation between the two-way source wavefield and the two-way receiver wavefield produces artifacts, many of which have low-frequency features. Many methods for addressing this problem have been proposed (Leveille et al., 2011). The Laplacian operator (Youn and Zhou, 2001; Zhang and Sun, 2009) can be used to process RTM images, effectively attenuating low-frequency artifacts. Mulder and Plessix (2003, 2004) use a high-pass filter to address low-frequency artifacts. Fletcher et al. (2005, 2006) introduce sponge boundary conditions in the nonreflection wave equation to attenuate reflected waves, thereby reducing the artifacts in RTM images. Yoon and Marfurt (2006) propose a new imaging condition with propagation angle constraints using the Poynting vector, which eliminated false imaging at nonreflecting points. Guitton et al. (2007) propose a least-squares filtering method that removes low-frequency artifacts while maintaining accurate imaging results. Liu et al. (2007, 2011) apply various techniques, such as the Hilbert transform, to replace the crosscorrelation of the two-way wavefields with the directed crosscorrelation of the one-way wavefields, which prevents the generation of artifacts in the RTM process. Based on the previous research, Fei et al. (2015) propose a de-primary imaging condition with fewer wavefield components to address these artifacts. Rocha

Manuscript received by the Editor 17 March 2022; revised manuscript received 20 July 2022; published ahead of production 12 September 2022; published online 28 October 2022.
[1]University of Science and Technology of China, School of Earth and Space Sciences, Laboratory of Seismology and Physics of Earth's Interior, Hefei, China and University of Science and Technology of China, National Geophysical Observatory at Mengcheng, Hefei, China. E-mail: yuyuwei@mail.ustc.edu.cn; yxli2017@mail.ustc.edu.cn; xinmwu@ustc.edu.cn; xjia@ustc.edu.cn (corresponding author).

DOI:10.1190/geo2022-0159.1

et al. (2016) propose a new inner product technique for RTM and full-waveform inversion (FWI), which can attenuate reflection in any ideal direction to remove RTM artifacts.

At present, the aforementioned methods for removing the RTM artifacts satisfy different detection requirements. The main impediment to the widespread adoption of regular RTM is the high computational cost (Etgen et al., 2009; Zhang and Sun, 2009; Leveille et al., 2011). It takes a considerable amount of time to calculate the two-way wavefields, and the extensive writing and reading operations require a large amount of storage space. Some methods for removing the artifacts (Fletcher et al., 2005, 2006; Yoon and Marfurt, 2006; Guitton et al., 2007; Liu et al., 2007, 2011; Fei et al., 2015; Rocha et al., 2016) also require substantial computational costs. Griewank (1992) proposes a checkpointing algorithm for reducing the storage required by writing and reading operations, and the few stored checkpoint wavefields could be used to reconstruct any wavefield. Griewank and Walther (2000) develop an optimized checkpointing method that greatly reduces the memory requirements while slightly increasing the computational load. Symes (2007) introduces this optimal checkpointing technology (Griewank and Walther, 2000) into RTM, which reduces the reliance of RTM on disk input/output. Anderson et al. (2012) present a modified version of the optimal checkpointing technology (Griewank and Walther, 2000) for isotropic elastic RTM and anisotropic viscoelastic FWI. For wavefield reconstruction in attenuated media, Yang et al. (2016) propose a checkpointing-assisted technique that requires less wavefield information than the optimal checkpointing technique. Although these methods can address the issue of limited computer memory, the large computational load of RTM remains a challenge. To reduce the computational cost, Morton and Ober (1998), Jing et al. (2000), and Zhao et al. (2016) propose methods for loading multiple pairs of seismic sources and recording data simultaneously in one migration. Due to the mismatch between the shot and the shot gather, the migration image often includes noise and crosstalk artifacts. Perrone and Sava (2012) propose a hybrid encoding method that combined the advantages of random shot-encoding migration and plane-wave migration. Their method maintains the resolution of traditional RTM while reducing noise in the images. Jia et al. (2020) develop a supervirtual shot-encoding scheme to attenuate artifacts in the simultaneous migration of multishot-gather data. This method has higher computational efficiency than plane-wave encoding methods.

Solving the wavefield in only one direction (Claerbout, 1970; Stoffa et al., 1990; Ristow and Rühl, 1994) can significantly reduce the calculation time. However, the limited wavefield propagation angle of the one-way wave propagator introduces large migration errors. Ristow and Rühl (1994) propose a hybrid migration method that combines phase-shift migration and finite-difference schemes; this method can be applied with relatively large velocity variations and steeply inclined structures. To expand the propagation angle of one-way elastic waves in arbitrarily heterogeneous media, Wu (1994) develops a thin-slab formulation of one-way elastic wave equations. Grimbergen et al. (1998) propose a modal expansion method to construct an intrinsically stable one-way wave propagator, which can improve the lateral resolution of migration. Xie and Wu (1998) use the Padé approximation to deal with the one-way wave equation and propose a new screen method. The proposed generalized screen propagator (GSP) simulates the wavefield relatively accurately with high velocity contrast and has a larger propagation angle than the previous screen propagator. Huang et al. (1999) propose an extended Born Fourier migration to address the instability of the application caused by the singularity problem and to accurately handle the steep interface problem. Zhang and Yao (2011) propose a compensation scheme with high computational efficiency to reduce the numerical dispersion and two-way splitting error of the finite-difference method. Based on the Chebyshev polynomials, Zhang et al. (2010) and Song et al. (2022) develop new Fourier propagators with propagation angles greater than 60° within 1% phase error. Sandberg and Beylkin (2009) use spectral projectors to remove the evanescent waves in full-wave equation extrapolation, and their method preserves wave propagations at all angles. You et al. (2020) use the derivative of the one-way wavefield to depth to realize the full-wave equation depth migration. Jia and Wu (2009) develop a super-wide angle one-way wave propagator to simulate turning waves. The migration based on their propagator could image overhanging structures. However, although one-way wave migration has been fully developed, it still faces various problems (Etgen et al., 2009; Zhang and Sun, 2009; Leveille et al., 2011): amplitude and phase inaccuracy, low resolution, and difficulty imaging large angle interfaces.

Deep learning is an artificial intelligence technology in computer science that can identify data features and potentially replace humans to complete tasks efficiently (Ronneberger et al., 2015; Sun et al., 2017; Shi et al., 2019; Wu et al., 2020). In addition, deep learning can be effective for problems that people cannot easily solve (Richardson and Feller, 2019; Yi and Bui, 2020; Avila et al., 2021; Zhang et al., 2021). As deep learning has developed, it has become widely used in various fields. Ronneberger et al. (2015) use convolutional neural networks (CNNs) to segment images of biological cells, and the network accurately delineates the cell boundaries. The U-shaped network (U-net) structure designed has been widely used in other studies. Sun et al. (2017) build a highly accurate deep learning model for plant classification. Yi and Bui (2020) apply deep learning to predict traffic congestion. In the field of geophysics, Richardson and Feller (2019) use a U-net for seismic data denoising. Wu et al. (2020) use a CNN for geologic interpretation and accurately identify fault locations. Zhang et al. (2021) use a CNN for least-squares RTM to reduce computational costs. Avila et al. (2021) propose a migration deconvolution method that fits the inverse operator with a U-net rather than calculating the inverse Hessian matrix. This method has a higher resolution than the Hessian filter least-squares migration method. In addition, deep learning has been successfully applied to inversion (Yang and Ma, 2019; Li et al., 2020; Wang et al., 2021), sparse data imaging (Huang and Nowack, 2020), and first-break picking (Yuan et al., 2018). Due to its wide applicability and perfect performance, deep learning has broad application prospects in the field of geophysics.

In this paper, we propose a CNN-based method for enhancing one-way wave equation-based migration images. Our network is a U-net with residual neural networks (ResNets). We use the RTM result based on the two-way wave propagator as the label of our network. The input is the one-way wave equation-based migration result. The one-way wave propagator is realized by a GSP. The GSP-based migration is faster than RTM. We intend to use the trained network to compensate for the image amplitude and phase defects of GSP-based migration.

THEORY

Two-way wave equation-based migration

Seismic vibration is an intuitive manifestation of seismic wave propagation, and the propagation of underground seismic waves

DOI:10.1190/geo2022-0159.1

can be expressed by wave equations. The 2D acoustic wave equation can be written as

$$\begin{cases} \frac{\partial u(x,z,t)}{\partial t} + \rho v^2(x,z)\left[\frac{\partial s_x(x,z,t)}{\partial x} + \frac{\partial s_z(x,z,t)}{\partial z}\right] = 0 \\ \rho \frac{\partial \mathbf{s}(x,z,t)}{\partial t} + \nabla u(x,z,t) = 0 \end{cases}, \quad (1)$$

where $u(x,z,t)$ and t are the acoustic wavefield and time, respectively; x and z are the spatial coordinates in the horizontal and vertical directions, respectively; ρ and $v(x,z)$ represent the density and acoustic velocity, respectively; the particle vibration velocity field has the form $\mathbf{s}(x,z,t) = (s_x(x,z,t), s_z(x,z,t))$; and ∇ is the gradient operator. In this work, the derivatives with respect to time and space in equation 1 are approximated by the Taylor series. The time derivative has the second-order precision, whereas the spatial derivative has the fourth-order precision. The final image is produced by applying the imaging condition to the finite-difference simulated wavefields.

We use RTM to generate the label image of the CNN; the RTM imaging condition is

$$I(x,z) = \int_0^T u_s(x,z,t) u_g(x,z,T-t) dt, \quad (2)$$

where $I(x,z)$ denotes the imaging result; dt refers to the time interval; $u_s(x,z,t)$ and $u_g(x,z,T-t)$ represent the forward-propagation wavefield of the source and the backward-propagation wavefield of the recorded data, respectively; and T is the total time of the recorded data. In this paper, we use the Laplacian filter (Youn and Zhou, 2001) to suppress the low-frequency artifacts of RTM.

One-way wave equation-based migration

In the frequency domain, the 2D acoustic wave equation can be expressed in the following form:

$$\left(\frac{\partial^2}{\partial x^2} + k_r^2 r^2\right) u(x,z) + \frac{\partial^2 u(x,z)}{\partial z^2} = 0, \quad (3)$$

where $k_r = \omega / v_r$ is the reference wavenumber; ω and v_r are the angular frequency and the reference velocity, respectively; and $r = v_r / v$ is the refraction index. Allowing for only the one-way wavefield, we decompose equation 3 and obtain the one-way wave equation of the forward propagation as

$$\frac{\partial u(x,z)}{\partial z} = i\sqrt{\frac{\partial^2}{\partial x^2} + k_r^2 r^2} u(x,z), \quad (4)$$

where i is the imaginary unit. We use the first-order Padé approximation to approximate the square root term of equation 4, yielding (Xie and Wu, 1998)

$$\frac{\partial u(x,z)}{\partial z} = i r k_r \left[1 + \frac{\frac{1}{2}\frac{1}{k_r^2 r^2}\frac{\partial^2}{\partial x^2}}{1 + \frac{1}{4}\frac{1}{k_r^2 r^2}\frac{\partial^2}{\partial x^2}}\right] u(x,z). \quad (5)$$

According to Fourier transform,

$$u(x,z) = \int dk_x p(z,k_x) e^{ik_x x}, \quad (6)$$

where k_x represents the x-direction wavenumber and $p(z,k_x)e^{ik_x x}$ refers to a part of the wavenumber-domain wavefield. According to equations 5 and 6, we have

$$p(z_1,k_x) = \exp\left\{ i\left[dzk_z - dzk_r\left(\frac{\delta v}{v} * \right) - dzk_r A \frac{k_x^2}{k_r^2}\right]\right\} p(z_0,k_x), \quad (7)$$

where dz is the spatial distance between z_1 and z_0; $A = 0.5[(1/r*) - 1]$; $r*$ is obtained from the Fourier transform of r, where $*$ is the wavenumber-domain convolution; $\delta v = v - v_r$ is the velocity perturbation; and k_z is the z-direction wavenumber. The right side of equation 7 includes three parts: the first two parts represent the phase screen solution and the third part is a modifier that allows the propagator to adapt to large velocity perturbations and wide propagation angles. To increase the computational efficiency, equation 7 can be converted to a dual-domain format (Xie and Wu, 1998):

$$p(x,z_1) = \left[1 + idz\frac{A}{k_r}\frac{\partial^2}{\partial x^2}\right] \times \mathrm{F}^{-1}\left[e^{idzk_z}\mathrm{F}\left[e^{-idzk_r\frac{\delta v}{v}} p(x,z_0)\right]\right], \quad (8)$$

where F[.] represents the Fourier transform and F^{-1}[.] represents the inverse Fourier transform. The GSP proposed in equation 8 can be used to simulate wavefields in media with strong local velocity perturbations. The GSP models wide-angle wavefields with relatively high accuracy and therefore can be used for migration. However, the GSP is a one-way wave propagator, and thus its accuracy for wavefield simulations is lower than that of the two-way wave propagator.

We use the zero-lag crosscorrelation imaging condition in the frequency domain:

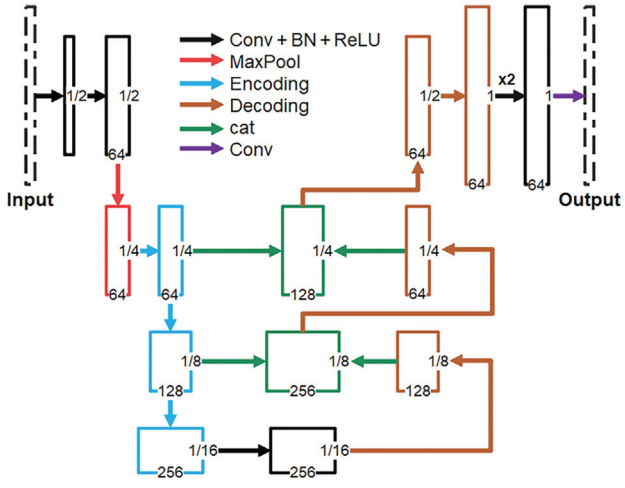

Figure 1. The topology of U-net1. In each rectangular frame, the horizontal annotation represents the number of channels and the vertical annotation represents the ratio of the size of the current image to the size of the original image. Conv, convolution; BN, batch normalization; ReLU, rectified linear unit activation function; MaxPool, max pooling; and cat, concatenation.

DOI:10.1190/geo2022-0159.1

$$I'(x,z) = \sum_{\omega} p_s(x,z,\omega) p_g^{\diamond}(x,z,\omega), \tag{9}$$

to obtain the input image of the CNN, where $p_s(x,z,\omega)$ and $p_g(x,z,\omega)$ are the forward-propagated source wavefield and the backward-propagated receiver wavefield, respectively, and $\diamond$ represents the complex conjugate.

U-net for enhancing one-way wave equation-based migration image

The image produced by one-way wave equation-based migration can be regarded as

$$P_1 = I_1 + \alpha, \tag{10}$$

where P_1 denotes the actual image obtained by one-way wave migration, I_1 is the corresponding true image, and α represents the artifacts and errors. Similarly, the image produced by two-way wave equation-based migration can be expressed as

$$P_2 = I_2 + \beta, \tag{11}$$

where P_2 is the actual RTM result and I_2 and β represent the true image and the RTM artifacts, respectively. To reduce the influence of β on P_2 as much as possible, we use the Laplacian filter (Youn and Zhou, 2001) to attenuate the artifact β.

We use a U-net to establish the mapping relationship from P_1 to P_2. The label of the U-net is the image produced by two-way wave migration, and the input is the result produced by one-way wave migration. Here, β is greatly attenuated by the Laplacian filter. In addition, because I_1 and α have almost no similarities to β, it is difficult to capture the similarities by the U-net and use them to create $I_1 - \beta$ and $\alpha - \beta$ connections; therefore, the mapping relationship from P_1 to P_2 is essentially the mapping relationship from P_1 to I_2. Thus, training the U-net is similar to fitting a function f, and we have

$$I_2 = f(P_1) = f(I_1 + \alpha). \tag{12}$$

Because α and I_2 share almost no structural similarities, the ideal function f removes α and corrects I_1 to ensure that it is as similar to I_2 as possible.

We train and validate two networks (U-net1 and U-net2) with different depths for comparison. The U-net topologies are shown in Figures 1 and 2. The U-net structure can be divided into two main components: downsampling and upsampling. In Figure 2, the structure of the encoding block is displayed in the azure rectangle. The different encoding blocks are ResNets with different convolution kernels or weights. The ResNets are introduced to solve the degradation problem caused by the increased network depth, allowing the CNN to increase the depth to extract more target features and become easier to optimize. The mapping that results due to the addition of the ResNets is sensitive to changes in the output. The network inside the brown rectangle in Figure 2 represents the decoding block, with the interpolation function and different ResNets forming different decoding blocks. U-net structures can identify target characteristics at different scales. The skip concatenations introduce original features with different scales to restore the target scale, and these original features can modify the output of the network.

Three loss functions are used to train U-net1 and U-net2: the mean absolute error (MAE), the mean-squared error (MSE), and SmoothL1. These loss functions are expressed in equations 13, 14, and 15, respectively. Here, m and n denote the outputs and labels of the CNN, respectively; q is the total number of elements in a batch; and θ is a variable that can be selected by the user. Due to the limitation of GSP's one-way attribute, GSP-based migration images contain many artifacts and outliers. At the beginning of training, these outliers are likely to be passed to the network output, causing

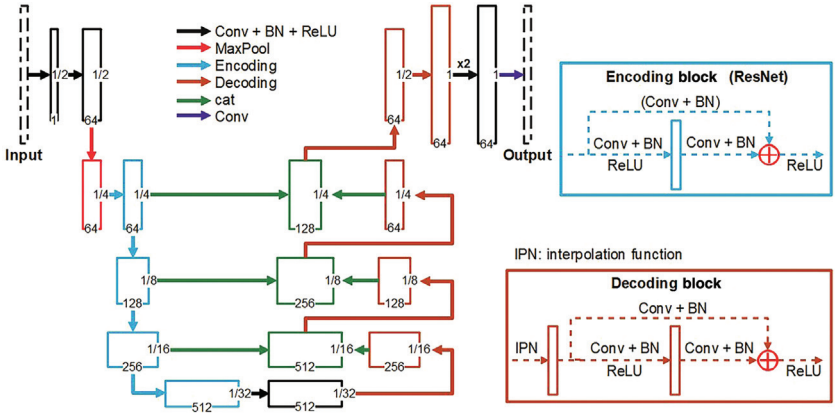

Figure 2. The topology of U-net2. The details of the encoding and decoding blocks are shown in the azure and brown rectangles, respectively. In the encoding blocks, a ResNet acts as an encoding block; these ResNets have the same structure and different convolution kernels or weights. The image size determines whether the operations in the parentheses are performed. An encoding operation consists of a certain number of encoding blocks. The decoding block consists of an interpolation (IPN) function and a ResNet.

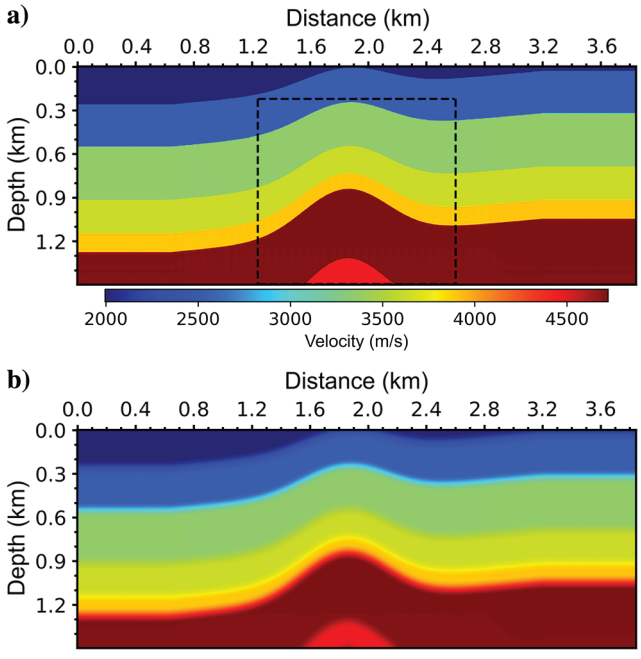

Figure 3. (a) True velocity model and (b) migration velocity model.

the MSE network to be unstable. However, the MSE network has a relatively stable gradient when the loss is close to zero as well as a relatively fast convergence speed. The l_1 norm of the difference between the output and the label is insensitive to outliers in the output. Nonetheless, it is difficult for the MAE network to calculate an effective gradient when the loss is close to zero. If we choose a reasonable θ, the SmoothL1 network has the advantages of the first two networks (Girshick, 2015)

$$\mathrm{MAE}(m,n)=\frac{1}{q}\sum_{j=1}^{q}|m_j-n_j|, \tag{13}$$

$$\mathrm{MSE}(m,n)=\frac{1}{q}\sum_{j=1}^{q}(m_j-n_j)^2, \tag{14}$$

$$\mathrm{SmoothL1}(m,n)=\begin{cases}\frac{1}{q}\sum_{j=1}^{q}[0.5(m_j-n_j)^2/\theta], & \text{if } |m_j-n_j|<\theta\\ \frac{1}{q}\sum_{j=1}^{q}[|m_j-n_j|-0.5\theta], & \text{otherwise}\end{cases}. \tag{15}$$

DATA SET ESTABLISHMENT

Migration image

Because our neural network models are designed to act on migration images, we need to compute the migration images to build the data set. A true velocity model is shown in Figure 3a. Figure 3b depicts a smooth version of the model, which is used for migration. We use the true model to generate synthetic data. The source is defined by a Ricker wavelet with a dominant frequency of 25 Hz. The grid spacing is 5 m. The source is distributed across the surface, with a source spacing of 80 m. Geophones are distributed on both sides of the source with a spatial interval of 5 m and a maximum offset of 2.5 km. We crop the adequately illuminated part of the RTM image to use as a high-quality label. Similarly, the input is a cropped GSP-based migration image. It should be noted that all of the images and velocity models shown in the following have been freely cropped. Figure 4a shows the velocity model from the rectangular box in Figure 3a. The GSP-based migration image corresponding to Figure 4a is shown in Figure 4b, whereas Figure 4c displays the corresponding RTM image. The one-way wave equation-based migration image has some artifacts, and the structure at this depth is indistinct. Compared with the true model, the spatial position of the structure (such as the peak of the uppermost anticline) in the migration image

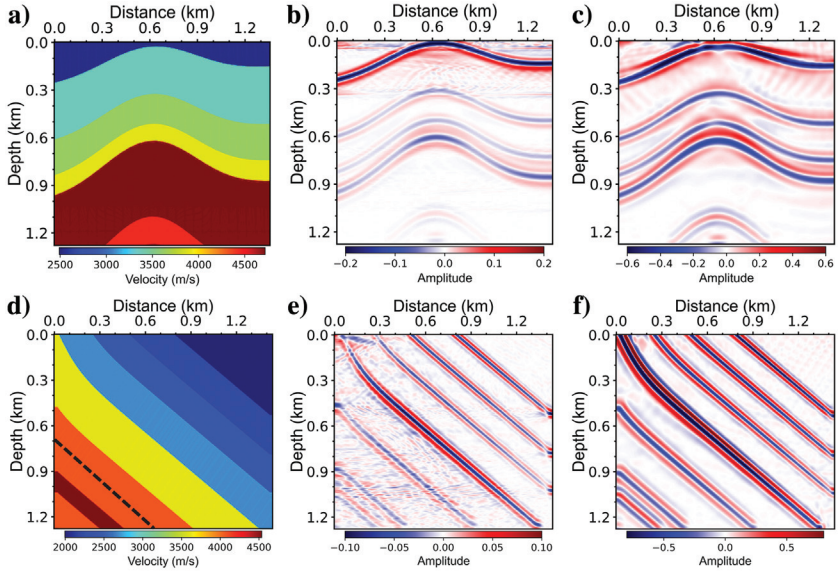

Figure 4. The velocity models and the results of one-way wave migration and RTM. (a) The rectangular area from Figure 3a, (b) the GSP-based migration image for the model shown in (a), (c) the RTM image for the model shown in (a), (d) a model including formations with large dips, (e) the GSP-based migration image for the model shown in (d), and (f) the RTM image for the model shown in (d).

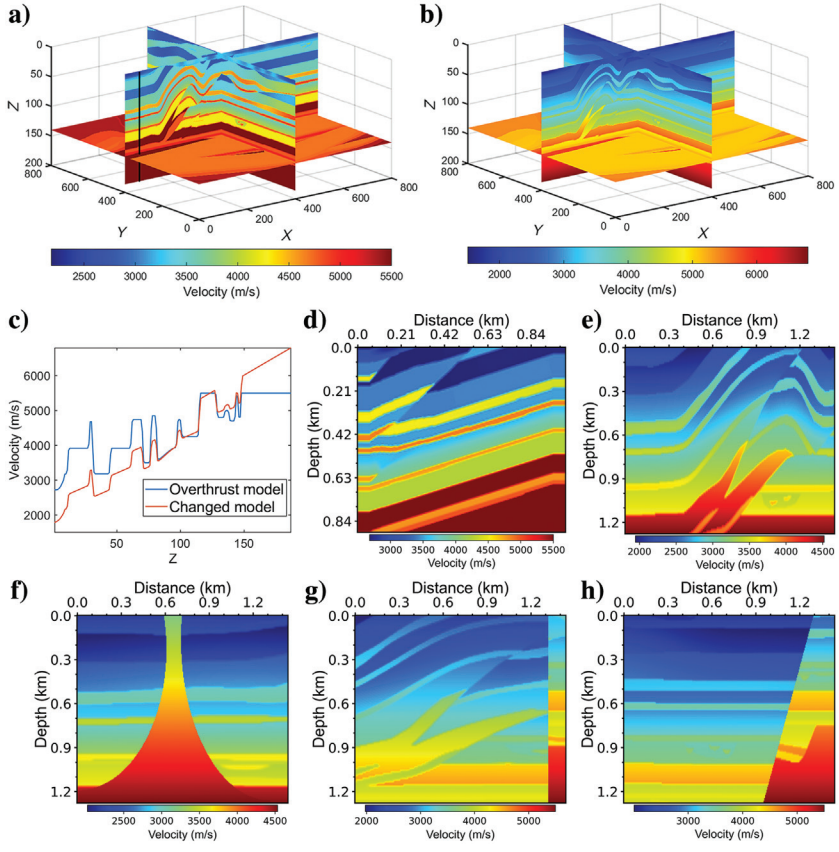

Figure 5. The SEG/EAGE overthrust model as well as its variant and slices. (a) The SEG/EAGE overthrust model, (b) a variant of the SEG/EAGE overthrust model, (c) the velocities extracted from the models shown in (a and b) along the black line indicated in (a), (d) slice model 1, (e) slice model 2, (f) slice model 3, (g) slice model 4, and (h) slice model 5.

is higher than the true position. These issues are not present in the two-way wave equation-based migration image.

When the model includes large inclination structures and severe lateral velocity variations, the wavefield and image calculated by GSP are biased. Figure 4e and 4f shows the GSP-based migration image and RTM image, respectively, for the model shown in Figure 4d. There are numerous artifacts in the GSP-based migration image. Most of these errors are caused by strong lateral velocity differences. In contrast, the RTM image is clear and has few artifacts. Low-frequency artifacts in the RTM image can be attenuated with a simple Laplacian filter. Due to the preceding features of the RTM image, we use RTM images as the labels in our work.

To ensure the richness of the U-net input samples, the migration parameters were defined with large ranges. The dominant frequency of the Ricker wavelet ranged from 17 to 40 Hz. The grid spacing (geophone spacing) ranged from 2.5 to 6 m. The maximum offset ranged from 1.5 to 3.5 km. The source spacing varied between 20 and 100 m.

Table 1. The proportion of different types of models.

	Type				
	T01	T02	T03	T04	T05
Proportion (%)	58.8	14.9	12.4	7.8	6.1

T01: simple models, such as those shown in Figure 4a and 4d; T02: models derived from the Marmousi model; T03: models derived from the overthrust model; T04: models with steep faults; and T05: models with steep salt domes.

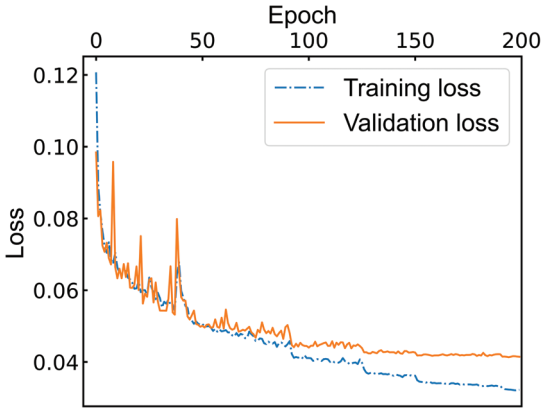

Figure 6. Loss convergence curves for the combination of U-net2 and SmoothL1.

Expansion of velocity models

Rich data sets are required for neural network training, verification, and testing. To expand the data sets, several velocity models have been developed. Some methods for expanding the velocity

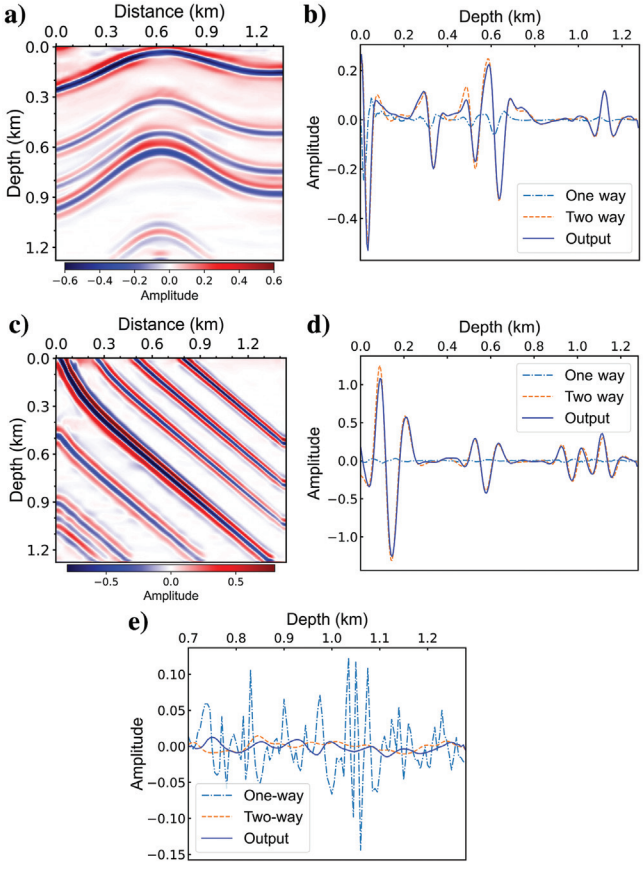

Figure 7. The CNN model outputs for the input shown in Figure 4. (a) The output for the input shown in Figure 4b; (b) the amplitudes of the images shown in Figure 4b, 4c, and (a) (distance = 0.7 km and depth = 0–1.28 km); (c) the output for the input shown in Figure 4e; (d) the amplitudes of the images shown in Figure 4e, 4f, and (c) (distance = 0.1 km and depth = 0–1.28 km); and (e) the amplitudes extracted from the images shown in Figure 4e, 4f, and (c) along the dashed black line indicated in Figure 4d (note that the image amplitudes are normalized to facilitate comparison of the relative magnitude of artifacts).

Table 2. The average losses and SSIMs of different combinations for the validation and test sets.

	U-net1			U-net2		
Outputs	MAE	MSE	SmoothL1	MAE	MSE	SmoothL1
Average loss	0.0555 ± 0.0001	0.0633 ± 0.0001	0.0634 ± 0.0001	0.0533 ± 0.0001	0.0581 ± 0.0001	0.0527 ± 0.0001
Average SSIM	0.91 ± 0.01	0.90 ± 0.01	0.89 ± 0.01	0.92 ± 0.01	0.91 ± 0.01	0.92 ± 0.01

To facilitate comparison, the output losses are uniformly calculated based on the MAE; the corresponding average SSIM of the inputs is 0.23.

models include cropping, rotation, vertical (or horizontal) interpolation, vertical (or horizontal) flips, and outward expansion (by horizontally copying the value of the model boundary). We apply one or more of these operations to enrich our model.

Figure 5a shows the SEG/EAGE overthrust model, whereas Figure 5b depicts its variant. Figure 5c exhibits the velocities extracted from the overthrust model and its variant along the black line in Figure 5a. Compared with the overthrust model, its variant has a wider velocity range and a larger average velocity gradient, allowing RTM to image steep structures. Based on the overthrust model and its variant, we have designed the models shown in Figure 5d and 5e. Moreover, we also have introduced some special structures into the generated models, as shown in Figure 5f–5h.

Our model library also includes models based on the benchmark Marmousi model. The models discussed previously are only a subset of our model library, with each type of model occupying a reasonable proportion of the library. The detailed proportions are shown in Table 1.

TRAINING AND VALIDATION

U-net1 and three loss functions are combined individually for training and validation, with the same operations applied to U-net2. We have 2889 pairs of input and label, of which the validation set accounts for approximately 10% and the rest is the training set. We use PyTorch version 1.10.0 on a GeForce RTX 3090 graphics processing unit (GPU) for training and validation. The average losses of different combinations for the validation and test sets after 200 epochs of training are provided in Table 2. To facilitate comparison, the average losses are uniformly calculated based on the MAE. To quantitatively evaluate the effectiveness of different combinations, the structural similarity index measure (SSIM) is introduced (Avila et al., 2021) by

$$\mathrm{SSIM} = \frac{(2\mu_o\mu_l + C_1)(2\sigma_{ol} + C_2)}{(\mu_o^2 + \mu_l^2 + C_1)(\sigma_o^2 + \sigma_l^2 + C_2)}, \tag{16}$$

where μ_o and μ_l are the mean values of o and l, respectively; σ_{ol} represents their covariance; and σ^2 represents the variance. In addition, $C_1 = (0.01L)^2$ and $C_2 = (0.03L)^2$, where L is the value range of the image amplitude. Here, l represents the CNN label and o refers to either the output or the input. For the validation and test sets, the average SSIM of the inputs is 0.23. The corresponding average SSIMs for the outputs of different combinations are shown in Table 2. The model with U-net2 and SmoothL1 has the lowest average loss and the highest average SSIM. The model with U-net2 and SmoothL1 greatly improves the average SSIM of the inputs. The convergence curve of this model during training is shown in Figure 6.

RESULTS

To generate the results for the validation and test sets, the U-net2 model with SmoothL1 is the ideal CNN model. Figure 7a shows the output of the network for the migration image in Figure 4b. Compared with the input, the deep structures are visible in the output. Figure 7b shows the amplitudes extracted along the line (distance = 0.7 km and depth = 0–1.28 km) in the migration images in Figures 4b, 4c, and 7a. Compared with the input, the output has an improved amplitude that essentially corresponds to the amplitude of the label. The same situation can be observed in Figures 4e, 4f, 7c, and 7d. In addition, the trained network effectively removes the artifacts in the input shown in Figure 4e caused by the large horizontal velocity perturbations, and thus the output

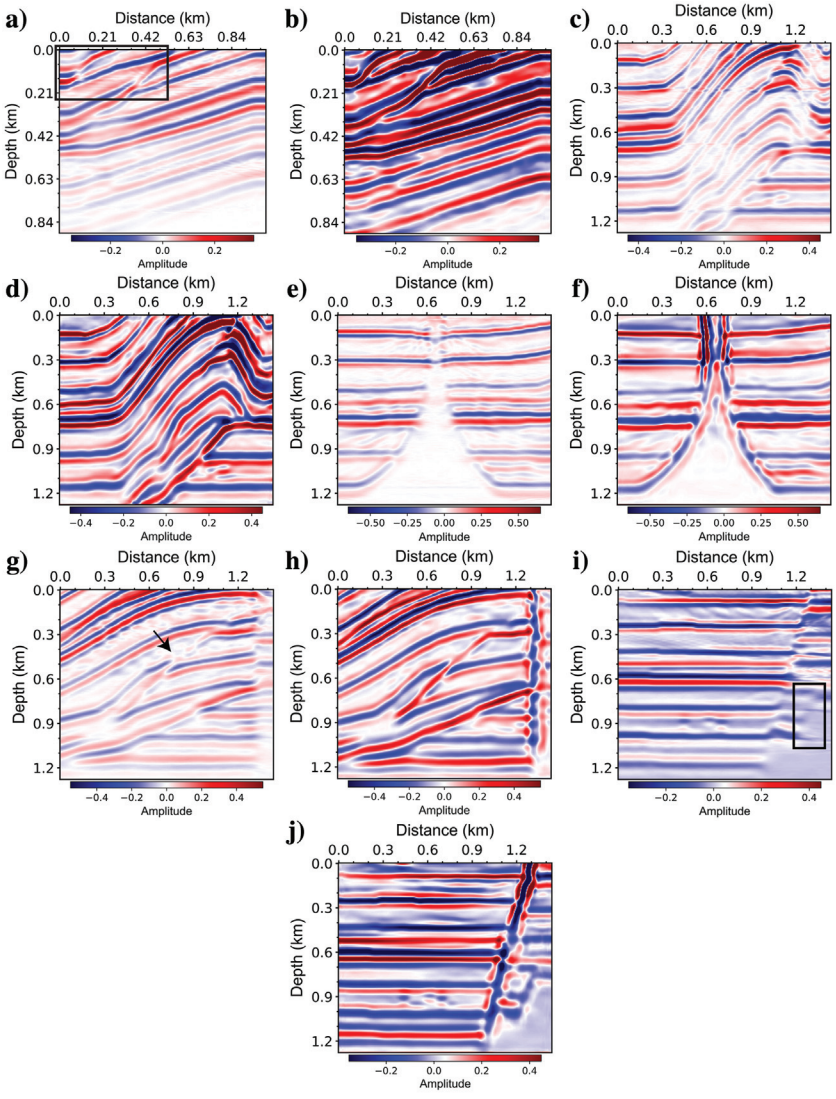

Figure 8. The inputs and outputs for the models displayed in Figure 5. (a) The GSP-based migration result for the model in Figure 5d, (b) the output for the input shown in (a), (c) the GSP-based migration result for the model in Figure 5e, (d) the output for the input shown in (c), (e) the GSP-based migration result for the model in Figure 5f, (f) the output for the input shown in (e), (g) the GSP-based migration result for the model in Figure 5g, (h) the output for the input shown in (g), (i) the GSP-based migration result for the model in Figure 5h, and (j) the output for the input shown in (i).

DOI:10.1190/geo2022-0159.1

shown in Figure 7c contains very few artifacts. There is no velocity difference at the position of the dashed black line in Figure 4d, in which the image amplitude should be zero. Figure 7e shows the amplitudes of the images displayed in Figures 4e, 4f, and 7c at this location, and it demonstrates that our method has the function of artifact attenuation.

The CNN model also performs well for complex models. Figure 5d depicts a fault model, and its GSP-based migration image is shown in Figure 8a. The image contrast at the bottom of Figure 8a is very low, and the fault in the black rectangular frame is unrecognizable. As shown in Figure 8b, our network model restores the fault structure and enhances the contrast in the deep area. When the formation has a very large inclination (Figure 5e), GSP-based migration has difficulty recovering the structure (Figure 8c). In the input image, the inclined strata are visually separated, and it is difficult to determine whether the structures between the separated strata are artifacts. Figure 8d shows how our CNN model recovered the fault structure displaying a clear image. High-velocity anomalies such as salt domes often have steep boundaries and strong velocity contrast, as shown in Figure 5f, and imaging these structures with one-way wave equation-based migration is challenging. The GSP-based migration image shown in Figure 8e has had difficulty restoring the steep boundaries. However, in the network output result (Figure 8f), the boundaries are clearly recovered. Similarly, the CNN model can reconstruct images of steep fault planes. Figure 8g and 8h and Figure 8i and 8j depict two pairs of inputs and outputs with steep faults with the corresponding models shown in Figure 5g and 5h, respectively. Compared with the inputs, the output images of the steep interfaces are significantly improved. The structure indicated by the black arrow in Figure 8g is improved in Figure 8h. Furthermore, the image shown in the black rectangular frame in Figure 8i is clearly illustrated in Figure 8j.

Moreover, we use the CNN model to process a larger image. Figure 9a shows the Marmousi model, with Figure 9b depicting the corresponding GSP-based image. The images in the training set are all 256 × 288 (points). However, the size of the image in Figure 9b is 388 × 848. Our network structure has an implicit nature that can naturally handle images of any size. With the input in Figure 9b, we can obtain higher resolution output, as shown in Figure 9c. The images of the interfaces, especially near the red arrow in Figure 9a, have been enhanced. In the area below the arrow in the model, the output has fewer artifacts and clearer structures than the input. Figure 9d shows the corresponding RTM result, and Figure 9e–9h shows the magnifications of Figure 9a–9d in the red focus area shown in Figure 9a, respectively. Figure 9e–9h clearly shows that our method has a higher resolution than GSP-based migration and RTM in these cases. To verify the generalizability of our CNN model, we take the GSP-based migration image for a slice of the 3D SEG/EAGE salt model (Figure 10a) as the CNN input (Figure 10b). Note that our velocity model library does not cover the 3D SEG/EAGE salt model. The CNN output shown in Figure 10c has a higher resolution than the input, especially for the salt dome boundary indicated by the red arrows

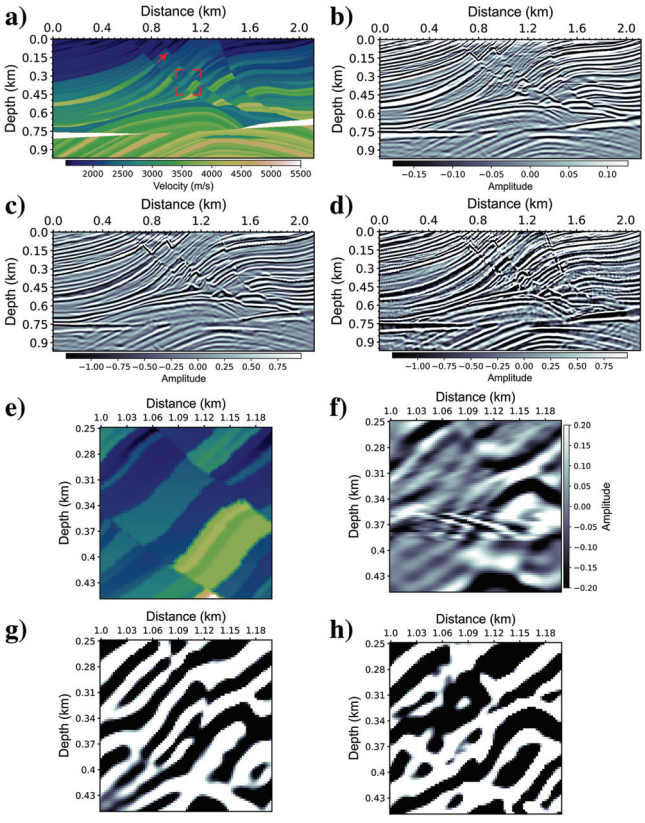

Figure 9. (a) The Marmousi model, (b) the GSP-based migration result, (c) the CNN output, (d) the RTM result, and (e–h) the magnifications of (a–d) in the red focus area shown in (a), respectively.

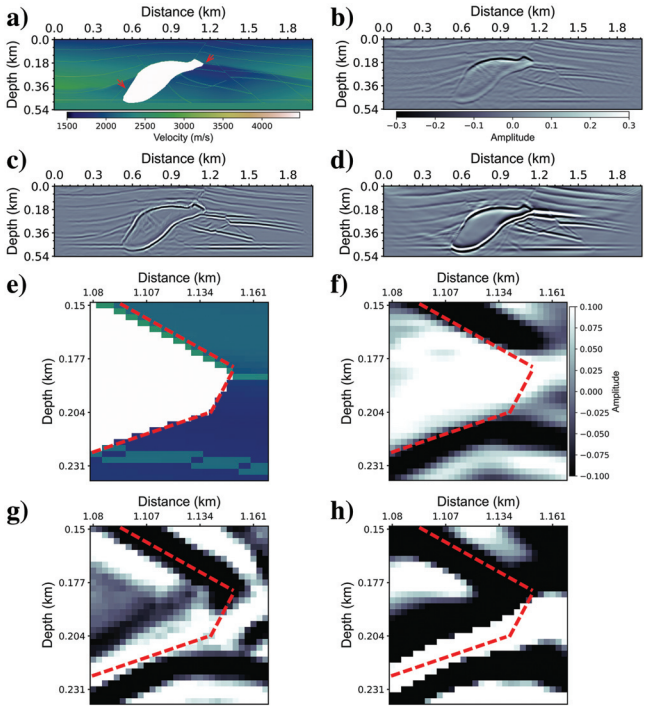

Figure 10. (a) A profile of the 3D SEG/EAGE salt model, (b) the GSP-based migration result, (c) the CNN output, (d) the RTM image, and (e–h) the magnifications of (a–d) in the area indicated by the upper red arrow in (a), respectively. Note the phase improvement of (g) compared with (f).

DOI:10.1190/geo2022-0159.1

Table 3. The SSIMs for the inputs and outputs of the velocity models.

	Figure (Model) label							
	4a	4d	5d	5e	5f	5g	5h	9a
Input	0.23 ± 0.01	0.08 ± 0.01	0.22 ± 0.01	0.23 ± 0.01	0.27 ± 0.01	0.20 ± 0.01	0.22 ± 0.01	0.03 ± 0.01
Output	0.96 ± 0.01	0.99 ± 0.01	0.91 ± 0.01	0.94 ± 0.01	0.94 ± 0.01	0.93 ± 0.01	0.94 ± 0.01	0.68 ± 0.01

shown in Figure 10a. Figure 10d exhibits the corresponding RTM image. Figure 10e–10h shows the magnifications of Figure 10a–10d in the area indicated by the upper red arrow in Figure 10a, respectively. The comparisons of Figure 10e–10h indicate that our method can improve the image of one-way wave equation-based migration. However, it is still challenging for the network to deal with such a steep and subtle salt boundary, allowing for absolutely nothing here in the input image.

The SSIMs of the preceding numerical examples are listed in Table 3. It is clear from Tables 2 and 3 that our network greatly improves the SSIMs between the GSP-based migration images and the RTM images. Thus, with our CNN model, the migration results based on the one-way wave propagator are as close as possible to the RTM results based on the two-way wave propagator.

Although the RTM can be used to accurately image complex structures, it has a considerable computational cost. The use of a one-way wave propagator rather than a two-way wave propagator for migration can save substantial calculation costs. With the same CPU usage, the calculation time of the RTM image is approximately 4.2 times that of the GSP-based migration image. Our CNN model generates an output from a GSP-based migration image in seconds. As discussed previously, the proposed method compensates for the shortcomings of one-way wave equation-based migration while saving considerable calculation costs in subsurface investigations.

CONCLUSION

We have proposed a method for improving one-way wave equation-based migration images by using CNN. The CNN mimics U-net and uses residual neural networks (ResNets) to improve its performance. The input of the network is the result of a one-way wave equation migration based on a GSP. The label is an RTM result, which has high imaging accuracy. We have tuned the network with different depths and different loss functions and tested the corresponding network models to obtain an ideal network model.

Although the GSP-based migration has lower calculation costs than RTM with a two-way wave propagator, it has difficulties handling steep structures and considerable velocity contrast. The ideal CNN model improves the resolution of the GSP-based migration image while removing the errors and artifacts caused by large horizontal velocity perturbations. Furthermore, because the proposed CNN model significantly mitigates amplitude deviations in the GSP-based migration image, the output image can precisely depict formations with large dips. With our CNN model, the GSP-based migration image is as close as possible to the RTM image, and the SSIM between the GSP-based migration result and the RTM result is improved. In addition to generating accurate imaging results, the computational burden of GSP-based migration with our CNN model is considerably lower than that of conventional RTM. The method described in this paper has potential applications in real-world subsurface investigations. In addition, our method provides a new CNN application mode that improves one migration method by learning from another one.

ACKNOWLEDGMENTS

This study is supported by the National Natural Science Foundation of China (nos. 42074125 and 41774121). We deeply thank the editors and three anonymous reviewers for helping us improve this paper.

DATA AND MATERIALS AVAILABILITY

Data associated with this research are available and can be obtained by contacting the corresponding author.

REFERENCES

Anderson, J. E., L. Tan, and D. Wang, 2012, Time-reversal checkpointing methods for RTM and FWI: Geophysics, **77**, no. 4, S93–S103, doi: 10.1190/geo2011-0114.1.

Avila, M. R. V., L. N. Osorio, J. de Castro Vargas Fernandes, A. Bulcão, B. Pereira-Dias, B. de Souza Silva, P. M. Barros, L. Landau, and A. G. Evsukoff, 2021, Migration deconvolution via deep learning: Pure and Applied Geophysics, **178**, 1677–1695, doi: 10.1007/s00024-021-02707-0.

Baysal, E., D. D. Kosloff, and J. W. C. Sherwood, 1983, Reverse time migration: Geophysics, **48**, 1514–1524, doi: 10.1190/1.1441434.

Claerbout, J. F., 1970, Coarse grid calculations of waves in inhomogeneous media with application to delineation of complicated seismic structure: Geophysics, **35**, 407–418, doi: 10.1190/1.1440103.

Etgen, J., S. H. Gray, and Y. Zhang, 2009, An overview of depth imaging in exploration geophysics: Geophysics, **74**, no. 6, WCA5–WCA17, doi: 10.1190/1.3223188.

Fei, T. W., Y. Luo, J. Yang, H. Liu, and F. Qin, 2015, Removing false images in reverse time migration: The concept of de-primary: Geophysics, **80**, no. 6, S237–S244, doi: 10.1190/geo2015-0289.1.

Fletcher, R. F., P. Fowler, P. Kitchenside, and U. Albertin, 2005, Suppressing artifacts in prestack reverse time migration: 75th Annual International Meeting, SEG, Expanded Abstracts, 2049–2051, doi: 10.1190/1.2148113.

Fletcher, R. P., P. J. Fowler, P. Kitchenside, and U. Albertin, 2006, Suppressing unwanted internal reflections in prestack reverse-time migration: Geophysics, **71**, no. 6, E79–E82, doi: 10.1190/1.2356319.

Girshick, R., 2015, Fast R-CNN: Proceedings of the IEEE International Conference on Computer Vision, 1440–1448.

Griewank, A., 1992, Achieving logarithmic growth of temporal and spatial complexity in reverse automatic differentiation: Optimization Methods and Software, **1**, 35–54, doi: 10.1080/10556789208805505.

Griewank, A., and A. Walther, 2000, Algorithm 799: Revolve: An implementation of checkpointing for the reverse or adjoint mode of computational differentiation: ACM Transactions on Mathematical Software, **26**, 19–45, doi: 10.1145/347837.347846.

Grimbergen, J. L. T., F. J. Dessing, and K. Wapenaar, 1998, Modal expansion of one-way operators in laterally varying media: Geophysics, **63**, 995–1005, doi: 10.1190/1.1444410.

Guitton, A., B. Kaelin, and B. Biondi, 2007, Least-squares attenuation of reverse-time-migration artifacts: Geophysics, **72**, no. 1, S19–S23, doi: 10.1190/1.2399367.

Huang, J., and R. L. Nowack, 2020, Machine learning using U-net convolutional neural networks for the imaging of sparse seismic data: Pure and Applied Geophysics, **177**, 2685–2700, doi: 10.1007/s00024-019-02412-z.

Huang, L.-J., M. C. Fehler, and R.-S. Wu, 1999, Extended local born Fourier migration method: Geophysics, **64**, 1524–1534, doi: 10.1190/1.1444656.

Jia, X., W. Chen, and B. Chen, 2020, An efficient super-virtual shot encoding scheme for multisource reverse time migration: Geophysics, **85**, no. 6, S405–S416, doi: 10.1190/geo2019-0479.1.

Jia, X., and R.-S. Wu, 2009, Superwide-angle one-way wave propagator and its application in imaging steep salt flanks: Geophysics, **74**, no. 4, S75–S83, doi: 10.1190/1.3124686.

Jing, X., C. J. Finn, T. A. Dickens, and D. E. Willen, 2000, Encoding multiple shot gathers in prestack migration: 70th Annual International Meeting, SEG, Expanded Abstracts, 786–789, doi: 10.1190/1.1816188.

Leveille, J. P., I. F. Jones, Z.-Z. Zhou, B. Wang, and F. Liu, 2011, Subsalt imaging for exploration, production, and development: A review: Geophysics, **76**, no. 5, WB3–WB20, doi: 10.1190/geo2011-0156.1.

Li, S., B. Liu, Y. Ren, Y. Chen, S. Yang, Y. Wang, and P. Jiang, 2020, Deep learning inversion of seismic data: IEEE Transactions on Geoscience and Remote Sensing, **58**, 2135–2149, doi: 10.1109/TGRS.2019.2953473.

Liu, F., S. A. Morton, J. P. Leveille, and G. Zhang, 2007, Reverse-time migration using one-way wavefield imaging condition: 77th Annual International Meeting, SEG, Expanded Abstracts, 2170–2174, doi: 10.1190/1.2792917.

Liu, F., G. Zhang, S. A. Morton, and J. P. Leveille, 2011, An effective imaging condition for reverse-time migration using wavefield decomposition: Geophysics, **76**, no. 1, S29–S39, doi: 10.1190/1.3533914.

McMechan, G. A., 1983, Migration by extrapolation of time-dependent boundary values: Geophysical Prospecting, **31**, 413–420, doi: 10.1111/j.1365-2478.1983.tb01060.x.

Morton, S. A., and C. C. Ober, 1998, Faster shot-record depth migrations using phase encoding: 68th Annual International Meeting, SEG, Expanded Abstracts, 1131–1134, doi: 10.1190/1.1820088.

Mulder, W. A., and R.-E. Plessix, 2003, One-way and two-way wave-equation migration: 73rd Annual International Meeting, SEG, Expanded Abstracts, 881–884, doi: 10.1190/1.1818081.

Mulder, W. A., and R.-E. Plessix, 2004, A comparison between one-way and two-way wave-equation migration: Geophysics, **69**, 1491–1504, doi: 10.1190/1.1836822.

Perrone, F., and P. Sava, 2012, Wave-equation migration with dithered plane waves: Geophysical Prospecting, **60**, 444–465, doi: 10.1111/j.1365-2478.2011.01011.x.

Richardson, A., and C. Feller, 2019, Seismic data denoising and deblending using deep learning, https://arxiv.org/abs/1907.01497, accessed 23 January 2022.

Ristow, D., and T. Rühl, 1994, Fourier finite-difference migration: Geophysics, **59**, 1882–1893, doi: 10.1190/1.1443575.

Rocha, D., N. Tanushev, and P. Sava, 2016, Acoustic wavefield imaging using the energy norm: Geophysics, **81**, no. 4, S151–S163, doi: 10.1190/geo2015-0486.1.

Ronneberger, O., P. Fischer, and T. Brox, 2015, U-net: Convolutional networks for biomedical image segmentation, *in* N. Navab, J. Hornegger, W. Wells, and A. Frangi, eds., Medical image computing and computer-assisted intervention, Lecture Notes in Computer Science 9351: Springer, 234–241, doi: 10.1007/978-3-319-24574-4_28.

Sandberg, K., and G. Beylkin, 2009, Full-wave-equation depth extrapolation for migration: Geophysics, **74**, no. 6, WCA121–WCA128, doi: 10.1190/1.3202535.

Shi, Y., X. Wu, and S. Fomel, 2019, SaltSeg: Automatic 3D salt segmentation using a deep convolutional neural network: Interpretation, **7**, no. 3, SE113–SE122, doi: 10.1190/INT-2018-0235.1.

Shragge, J., and G. Shan, 2008, Prestack wave-equation depth migration in elliptical coordinates: Geophysics, **73**, no. 5, S169–S175, doi: 10.1190/1.2956349.

Song, H., J. Zhang, and Y. Zou, 2022, Direct expansion of Fourier extrapolator for one-way wave equation using Chebyshev polynomials of the second kind: Geophysics, **87**, no. 2, S63–S73, doi: 10.1190/geo2021-0114.1.

Stoffa, P. L., J. T. Fokkema, R. M. de Luna Freire, and W. P. Kessinger, 1990, Split-step Fourier migration: Geophysics, **55**, 410–421, doi: 10.1190/1.1442850.

Sun, Y., Y. Liu, G. Wang, and H. Zhang, 2017, Deep learning for plant identification in natural environment: Computational Intelligence and Neuroscience, **2017**, 7361042, doi: 10.1155/2017/7361042.

Symes, W. W., 2007, Reverse time migration with optimal checkpointing: Geophysics, **72**, no. 5, SM213–SM221, doi: 10.1190/1.2742686.

Wang, W., G. A. McMechan, and J. Ma, 2021, Elastic isotropic and anisotropic full-waveform inversions using automatic differentiation for gradient calculations in a framework of recurrent neural networks: Geophysics, **86**, no. 6, R795–R810, doi: 10.1190/geo2020-0542.1.

Wu, R.-S., 1994, Wide-angle elastic wave one-way propagation in heterogeneous media and an elastic wave complex-screen method: Journal of Geophysical Research: Solid Earth, **99**, 751–766, doi: 10.1029/93JB02518.

Wu, X., Z. Geng, Y. Shi, N. Pham, S. Fomel, and G. Caumon, 2020, Building realistic structure models to train convolutional neural networks for seismic structural interpretation: Geophysics, **85**, no. 4, WA27–WA39, doi: 10.1190/geo2019-0375.1.

Xie, X.-B., and R.-S. Wu, 1998, Improve the wide angle accuracy of screen method under large contrast: 68th Annual International Meeting, SEG, Expanded Abstracts, 1811–1814, doi: 10.1190/1.1820283.

Yang, F., and J. Ma, 2019, Deep-learning inversion: A next-generation seismic velocity model building method: Geophysics, **84**, no. 4, R583–R599, doi: 10.1190/geo2018-0249.1.

Yang, P., R. Brossier, L. Métivier, and J. Virieux, 2016, Wavefield reconstruction in attenuating media: A checkpointing-assisted reverse-forward simulation method: Geophysics, **81**, no. 6, R349–R362, doi: 10.1190/geo2016-0082.1.

Yi, H., and K.-H. N. Bui, 2020, An automated hyperparameter search-based deep learning model for highway traffic prediction: IEEE Transactions on Intelligent Transportation Systems, **22**, 5486–5495, doi: 10.1109/TITS.2020.2987614.

Yoon, K., and K. J. Marfurt, 2006, Reverse-time migration using the pointing vector: Exploration Geophysics, **37**, 102–107, doi: 10.1071/EG06102.

You, J., J. Cao, and J. Wang, 2020, Two-way wave equation prestack depth migration using the matrix decomposition theory: Chinese Journal of Geophysics, **63**, 3838–3848, doi: 10.6038/cjg2020O0027.

Youn, O. K., and H.-W. Zhou, 2001, Depth imaging with multiples: Geophysics, **66**, 246–255, doi: 10.1190/1.1444901.

Yuan, S., J. Liu, S. Wang, T. Wang, and P. Shi, 2018, Seismic waveform classification and first-break picking using convolution neural networks: IEEE Geoscience and Remote Sensing Letters, **15**, 272–276, doi: 10.1109/LGRS.2017.2785834.

Zhang, J.-H., W.-M. Wang, S.-Q. Wang, and Z.-X. Yao, 2010, Optimized Chebyshev Fourier migration: A wide-angle dual-domain method for media with strong velocity contrasts: Geophysics, **75**, no. 2, S23–S34, doi: 10.1190/1.3350861.

Zhang, J.-H., and Z.-X. Yao, 2011, Reducing two-way splitting error of FFD method in dual domains: Geophysics, **76**, no. 4, S165–S175, doi: 10.1190/1.3590214.

Zhang, W., J. Gao, T. Yang, X. Jiang, and W. Sun, 2021, Least-squares reverse time migration using convolutional neural networks: Geophysics, **86**, no. 6, R959–R971, doi: 10.1190/geo2021-0006.1.

Zhang, Y., and J. Sun, 2009, Practical issues in reverse time migration: True amplitude gathers, noise removal and harmonic source encoding: First Break, **27**, 53–59, doi: 10.3997/1365-2397.2009002.

Zhao, Z., M. K. Sen, and P. L. Stoffa, 2016, Double-plane-wave reverse time migration in the frequency domain: Geophysics, **81**, no. 5, S367–S382, doi: 10.1190/geo2015-0687.1.

Biographies and photographs of the authors are not available.